SCIENTIFIC REPORTS

OPEN

Enhanced-contrast optical readout in ultrafast broadband Raman quantum memories

A. M. Zheltikov[1,2,3,4]

The signal-to-noise contrast of the optical readout in broadband Raman quantum memories is analyzed as a function of the pulse widths and phase properties of tailored optical field waveforms used to write in and read out broadband photon wave packets. Based on this analysis, we quantify the tradeoff between the readout contrast and the speed of such memories. Off-resonance coherent four-wave mixing is shown to provide a source of noise photons, lowering the readout contrast in broadband Raman quantum memories. This noise cannot be suppressed by phase matching, but can be radically reduced with a suitable polarization arrangement and proper field-waveform tailoring.

Optical quantum memories – systems capable of storing and maintaining quantum states of light, releasing them on demand – are of central importance for the emerging photonic quantum technologies[1,2]. Highly promising approaches to optical quantum memory have been demonstrated using ultracold atoms[3], molecular gases[4], atomic vapors[5], rare-earth ion-doped crystals[6], as well as phonons in room-temperature diamond[7–13]. Raman processes in ensembles of cold atoms have been shown to offer unique quantum-memory modalities, enabling polarization entanglement storage, as well as heralded single-photon entanglement of path and polarization storage[14]. Remarkably long coherence times have been demonstrated for a variety of quantum-memory systems operated at low temperatures[2], including an astonishing six-hour coherence time in optically addressable nuclear spin systems in rare-earth ion-doped solids at 2 K[15], opening new horizons in long-distance quantum communications.

As an alternative strategy, broadband quantum states of light, including broadband single-photon wave packets can be stored and retrieved on demand using vibrational and rotational modes of molecules[4,16], as well as laser-driven phonons in diamond[7–13]. For this class of systems, coherence times are much shorter, typically ranging from a few picoseconds to several nanoseconds. However, unlike ultralong-coherence-time quantum memories, such shorter-lived memories can provide extremely broad, terahertz bandwidths and can function at room temperatures[7–13]. Moreover, such systems can operate at a much faster, femtosecond time scale, offering unique options for ultrahigh-speed quantum information technologies. Raman scattering provides an ideal write-in/read-out protocol for such broadband quantum memories[17–19], allowing the quantum states of photons to be mapped onto molecular modes in gases or phonons[20] in solids and enabling two-mode entanglement between light and relatively long-lived molecular or phonon modes in matter[21–23].

Here, we analyze the tradeoff between the rate at which broadband Raman quantum memories can operate and the signal-to-noise contrast of the anti-Stokes readout from such memories. In crystalline solids, the readout contrast is strongly anisotropic, spanning many orders of magnitude for various polarization arrangements of the optical fields. Off-resonance coherent four-wave mixing (FWM) will be shown to provide a source of noise photons, lowering the readout contrast in broadband Raman quantum memories. We will demonstrate that this noise cannot be suppressed by phase matching, but can be reduced by many orders of magnitude with suitable polarization arrangements and proper field-waveform tailoring.

[1]Department of Physics and Astronomy, Texas A&M University, College Station, 77843, Texas, USA. [2]Physics Department, International Laser Center, M.V. Lomonosov Moscow State University, Moscow, 119992, Russia. [3]Russian Quantum Center, Skolkovo, Moscow Region, 143025, Russia. [4]Kazan Quantum Center, A.N. Tupolev Kazan National Research Technical University, Kazan, 420126, Russia. Correspondence and requests for materials should be addressed to A.M.Z. (email: zheltikov@physics.msu.ru)
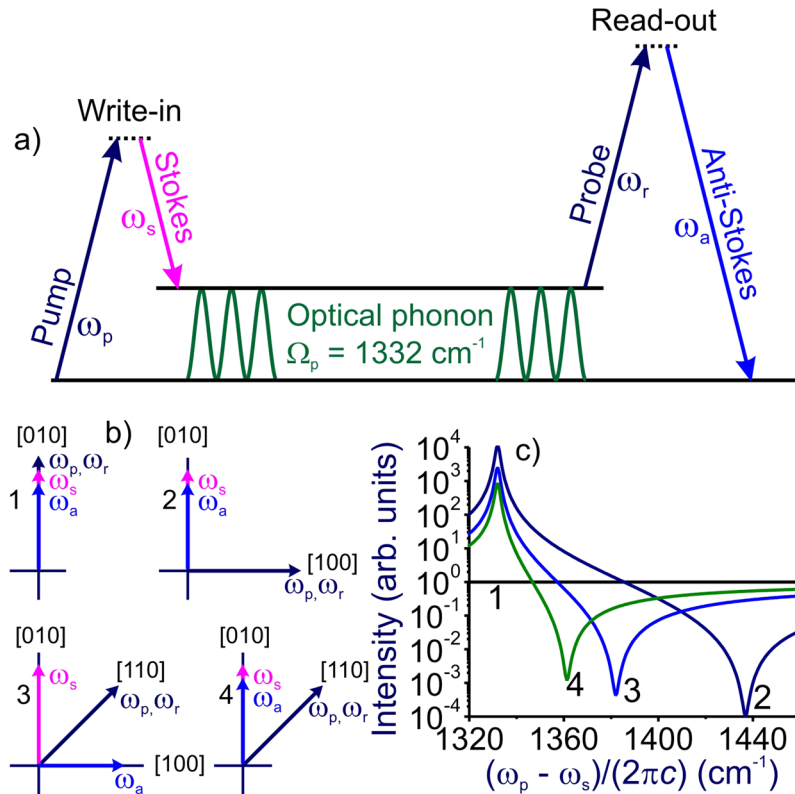
Figure 1. (**a**) Coherent anti-Stokes readout off the Raman quantum memory: (left) a frequency-tunable Stokes field maps the broadband pump wave packet into a memory based on coherently driven optical phonon, (right) the probe field applied with a variable delay time reads out the coherence driven by the pump and Stokes fields, giving rise to an anti-Stokes signal, which serves to report the state of the phonon memory. (**b**) Four polarization arrangements for the Raman quantum memory with anti-Stokes readout. Field polarization vectors are shown (arrows) against crystallographic directions. (**c**) The spectra of the anti-Stokes readout for different polarization arrangements as specified in panel (b) in the regime when the bandwidths of the pump, Stokes, and probe fields, Δ_p, Δ_s, and Δ_r, are much smaller than the linewidth Γ of the Raman mode.

Heisenberg-picture anti-Stokes readout analysis

We consider optical readout signal generation in a Raman quantum memory scheme as a result of two-step coherent anti-Stokes Raman scattering (CARS) process involving write-in and read-out stages (Fig. 1a). CARS has been shown to provide a versatile spectroscopic protocol for the optical interrogation of long-lived coherent phonon modes in solids[24–27], including the phonon modes in diamond, considered promising candidates for sold-state broadband memory[7–13]. At the first, write-in step, two fields with frequencies ω_p and ω_s, referred to, in accordance with the standard CARS nomenclature[28,29], as the pump and Stokes fields, drive a molecular or phonon mode with a central frequency Ω_R through a Raman-type resonance, $\omega_p - \omega_s \approx \Omega_R$. At the second step, a probe field with a frequency ω_r reads out the Raman coherence, giving rise to an anti-Stokes signal at the central frequency $\omega_a = \omega_p - \omega_s + \omega_r$, which serves to report the state of the phonon memory.

Field quantization is performed by replacing the slowly varying field envelopes $A(t, z)$ by operators

$$\hat{A}(t, z) = \left(\frac{\hbar\omega_0}{n_0 c}\right)^{1/2} \int \hat{a}(\omega)\exp[i(\beta_\omega z - \omega t)]d\omega,$$

(1)

where ω_0 is the central frequency of the wave packet, n_0 is the refractive index at the frequency ω_0, β_ω is the propagation constant at the frequency ω, and $\hat{a}(\omega)$ is the field annihilation operator such that $[\hat{a}(\omega), \hat{a}^\dagger(\omega')] = \delta(\omega - \omega')$.

The slowly varying field annihilation operator in the time domain is defined through the Fourier transform

$$\hat{a}(t, z) = \left(\frac{1}{2\pi}\right)^{1/2} \int \hat{a}(\omega, z)\exp[i(\beta_\omega z - \omega t)]d\omega,$$

(2)

where $\hat{a}(\omega, z) = \hat{a}(\omega)\exp(i\beta_\omega z)$, so that $[\hat{a}(\omega, z), \hat{a}^\dagger(\omega', z)] = \delta(\omega - \omega')$ and $[\hat{a}(t, z), \hat{a}^\dagger(t', z)] = \delta(t - t')$.

In the second-quantization picture, the evolution of a quantum memory based on a Raman-active phonon driven by a classical pump field with a spectrum $A_p(\omega)$ is described by an effective Hamiltonian[30]

$$\hat{H}' = \hbar g \hat{A}_s^{\dagger} \hat{Q}^{\dagger} + H.\,c., \tag{3}$$

where $\hat{Q}^{\dagger}$ is the phonon creation operator, $\hat{A}_s = \int \Theta(\omega) \hat{a}_s(\omega) d\omega$, $\hat{a}_s(\omega)$ is the Stokes-field annihilation operator, $\Theta(\omega) = A_p(\omega)[\int |A_p(\omega')|^2 d\omega']^{-1/2}$, $g = \vartheta[\int |A_p(\omega')|^2 d\omega']^{1/2}$, and ϑ is the effective coupling constant.

The properties of such a Hamiltonians are discussed in an extensive literature on Raman quantum memory (see, e.g., refs[17,18]), as well as Raman protocols of quantum communication and quantum information processing[31]. The main focus of this work is on the limitations on the contrast of the optical readout in broadband Raman quantum memories due to the unwanted coherent FWM originating from off-resonance-driven electronic and two-photon excitations. The nonlinear signal produced through such FWM processes interferes with the anti-Stokes readout from the Raman coherence, dramatically lowering its contrast. Central to the analysis of this interference in classical-field models and experiments is the dispersion of the Raman-resonance and nonresonant parts of the pertinent nonlinear susceptibility[28,29,32], that is, the frequency dependence of the Raman-resonant and nonresonant terms in the effective coupling constant. The goal of our analysis here is to extend these classical models to the Raman schemes operating with quantum states of the Stokes and anti-Stokes fields, such as Raman quantum memories. To this end, we continue treating the pump and readout (probe) fields classically and write the Hamiltonian as[33–35]

$$\hat{H} = \delta(\hat{a}_a^{\dagger}\hat{a}_a + \hat{a}_s^{\dagger}\hat{a}_s) + \kappa(\hat{a}_a^{\dagger}\hat{a}_s^{\dagger} + \hat{a}_a\hat{a}_s), \tag{4}$$

where $\hat{a}_{a,s} = \hat{a}(\omega_{a,s}, z)$ $\hat{a}_{a,s}^{\dagger} = \hat{a}^{\dagger}(\omega_{a,s}, z)$, $\delta = \Delta\beta/2 + \gamma(P_p + P_r)/2$, P_p and P_r are the peak powers of the pump and probe fields, $\Delta\beta = \beta_a + \beta_s - \beta_p - \beta_r$, $\beta_j = \beta(\omega_j)$, $j = $ p, s, r, a, $\kappa = \varepsilon\gamma A_p A_r$, ε is the polarization-sensitive numerical factor, P_p and P_r are the complex amplitudes of the pump and probe fields, respectively, and γ is the nonlinear coefficient related to the pertinent third-order optical susceptibility.

For the full quantum analysis of the phonon modes behind the quantum memory, the evolution equations as dictated by the Hamiltonian (3) need to be included in the model. The Hamiltonian (4) is not intended for such an analysis. Instead, it provides an adequate framework for the description of the spectral interference of the anti-Stokes readout from the Raman coherence with off-resonance FWM, thus enabling a quantitative analysis of the readout contrast in Raman quantum memories.

With the Hamiltonian taken in the form of Eq. (4), the solution to the Heisenberg-picture evolution equations

$$d\hat{a}_{a,s}/dz = i[\hat{a}_{a,s}, \hat{H}] \tag{5}$$

can be written in the input–output form as[33–35]

$$\hat{a}_a(z) = \mu(z)\hat{a}_a(0) + \nu(z)\hat{a}_s^{\dagger}(0), \tag{6}$$

$$\hat{a}_s^{\dagger}(z) = \mu^*(z)\hat{a}_s^{\dagger}(0) + \nu^*(z)\hat{a}_a(0), \tag{7}$$

where $\mu(z) = \cos(sz) + i(\delta/s)\sin(sz)$, $\nu(z) = i(\kappa/s)\sin(sz)$, and $s^2 = \delta^2 - \kappa^2$.

For a rigorous analysis of ultrashort pulses, the full spatial derivatives d/dz in the evolution equations for $\hat{a}_{a,s}$ should be replaced by convective derivatives $\partial/\partial z + u_{a,s}^{-1}\partial/\partial t$, with u_s and u_a being the group velocities of the Stokes and anti-Stokes pulses. Here, however, we seek to isolate effects related to the pulse shape, phase, and polarization of optical fields. We therefore choose to work in the approximation where group walk-off effects are neglected – approximation that is broadly accepted even in ultrafast-CARS literature[36].

We now use the Heisenberg picture to calculate the expectation value for the anti-Stokes field photon-number operator, $\langle n_a(z)\rangle = \langle\psi(z=0)|\hat{a}_a^{\dagger}(z)\hat{a}_a(z)|\psi(z=0)\rangle$. With an input Stokes–anti-Stokes field state with no anti-Stokes photons at $z=0$, $|\psi(z=0)\rangle = |s, 0\rangle$, we find

$$\langle n_a(z)\rangle = |\nu(z)|^2(\langle n_{s0}\rangle + 1), \tag{8}$$

where $\langle n_{s0}\rangle = \langle n_s(z=0)\rangle$.

Notably, with $<n_{s0}> = 0$, corresponding to a vacuum input state, $|\psi(z=0)\rangle = |0, 0\rangle$, Eq. (8) recovers the two-mode squeezed-state result of the input–output Heisenberg-picture analysis of FWM[33–35], $\langle n_a(z)\rangle = |\nu(z)|^2$.

It is, however, the first, $\propto <n_{s0}>$ term of Eq. (8) that we are mainly concerned with here in our analysis of broadband Raman quantum memories. For $|\kappa| \ll |\delta|$, this part of the anti-Stokes readout can be written as

$$R(z) = |\nu(z)|^2 \langle n_{s0}\rangle = |\gamma|^2 \frac{\sin^2(\Delta\beta z/2)}{(\Delta\beta/2)^2} P_p P_r \langle n_{s0}\rangle. \tag{9}$$

In the case of a classical Stokes field at the input, $\langle n_{a,s}\rangle \approx (\hbar\omega_{a,s})^{-1} P_{a,s}\tau_{a,s}$, where $P_{a,s}$ are the peak powers of the anti-Stokes and Stokes pulses and $\tau_{a,s}$ are their respective pulse widths, the standard classical-field result is recovered:

$$P_a(z) \propto |\gamma|^2 \frac{\sin^2(\Delta\beta z/2)}{(\Delta\beta/2)^2} \frac{\tau_s}{\tau_a} \frac{\omega_a}{\omega_s} P_p P_r P_s. \tag{10}$$

Off-resonance coherent four-wave mixing as a source of anisotropic photon noise

Apart from the complex, frequency-dependent Raman-resonant part, $\gamma_R(\omega)$, the FWM nonlinear coefficient γ generally includes a purely real nonresonant term, γ_{nr}, related to electron transitions[28,29,32,37], and may include a distinct two-photon-resonant term[38,39], γ_{tp}, which is of special significance in solid semiconductors,

$$\gamma = \gamma_R(\omega) + \gamma_{nr} + \gamma_{tp}. \tag{11}$$

For cubic and isotropic materials, the spectrum of the Raman resonance can be approximated with a Lorentzian profile, leading to the following three-term approximation for $|\gamma|^2$ near the Raman resonance $\omega_p - \omega_s \approx \Omega_R$[38,39]:

$$\left|\gamma(\omega_p - \omega_s)\right|^2 \propto \left|1 - i\frac{\chi_2}{\chi_1} + \frac{N|\alpha_R|^2}{4\hbar\chi_1}\frac{1}{\Omega_R - (\omega_p - \omega_s) + i\Gamma}\right|^2, \tag{12}$$

where N is the number density of Raman-resonant species, Γ is the linewidth of the Raman resonance, α_R is the local-field-corrected polarizability, χ_1 and χ_2 are the real and imaginary parts of the effective cubic susceptibility $\chi_{eff} = \chi_1 - i\chi_2$, which can be expressed through the components of the electronic third-order susceptibility $\chi_{ijkl}^{(3)E}$ as $\chi_{eff} = d_1\chi_{1111}^{(3)E} + d_2\chi_{1221}^{(3)E} + d_3\chi_{1122}^{(3)E}$. The coefficients d_1, d_2, and d_3 depend on the polarization arrangement of optical fields, reflecting tensor properties of the electronic susceptibility $\chi_{ijkl}^{(3)E}$ and polarizability α_R. For four representative arrangements of the pump, Stokes, probe, and anti-Stokes polarization vectors relative to the [100] direction of the diamond lattice sketched in Fig. 1, we find no Raman resonance for polarization geometry 1 (curve 1 in Fig. 1c), $d_1 = 0$, $d_2 = 6$, and $d_3 = 0$ for geometry 2 (curve 2 in Fig. 1c), $d_1 = 0$, $d_2 = 0$, and $d_3 = 12$ for geometry 3 (curve 3 in Fig. 1c), and $d_1 = 6$, $d_2 = 6$, and $d_3 = 0$ for geometry 4 (curve 4 in Fig. 1c).

The anti-Stokes signal is thus a result of spectral interference of the photon fields generated through the CARS-type scattering of the probe field off the Raman coherence, encoding the information written by the pump and Stokes fields, and the nonresonant FWM background related to the γ_{nr} and γ_{tr} terms in Eq. (11). Both the useful anti-Stokes Raman memory readout signal and the FWM background build up as $\sin^2(\Delta\beta z/2)$ as functions of the propagation path. As a consequence, the nonresonant background in anti-Stokes photon counts cannot be suppressed by phase-matching adjustments.

Polarization-sensitive anti-Stokes readout contrast enhancement

As can be seen from Eq. (12), the ratio $\eta = N|\alpha_R|^2/(4\hbar\chi_1)$ [the factor that appears in front of the frequency denominator in the third term in Eq. (12)] provides a meaningful quantitative measure for the contrast of the anti-Stokes memory readout relative to the FWM nonresonant background. This ratio is highly sensitive to the polarizations of the optical fields used to write information into the Raman memory and to read out the state of this memory.

Analysis of the tensor properties of $\chi_{ijkl}^{(3)E}$ and polarizability α_R of diamond shows that this material is, in many respects, a highly promising medium for quantum memory. The cubic symmetry of the crystal lattice of diamond provides an ample parameter space for η contrast optimization. At the same time, the 1332-cm^{-1} zone-center $\Gamma^{(25+)}$ (F_{2g}) symmetry optical phonon in diamond, offers an advantageous combination of a broad, terahertz bandwidth and a sufficiently long coherence time in the range of a few picoseconds, allowing ultrafast Raman memory schemes to be implemented at room temperatures using femtosecond laser pulses[7–13].

However, a great care needs to be exercised in choosing polarizations of the laser beam to provide the highest possible anti-Stokes-readout-to-FWM-background ratios. In particular, for the polarization arrangement where the pump field is polarized along the [100] direction of the diamond lattice, while the Stokes and probe fields are polarized along the [010] direction (polarization geometry 2 in Fig. 1b), we have $\eta \approx 110\,\text{cm}^{-1}$ and $|\chi_2/\chi_1| \ll 1$[38,39], providing a high-contrast anti-Stokes readout against a virtually negligible FWM background (curve 2 in Fig. 1c).

Storing polarization qubits, however, requires two different polarization arrangements of optical fields. Building upon the high η ratios provided by the polarization arrangement 2 in Fig. 1b, it is tempting to use a scheme with all the laser fields polarized along the [010] direction (polarization geometry 1 in Fig. 1b) as the second polarization arrangement for polarization-qubit storage. However, the triply degenerate F_{2g}-symmetry optical phonon in diamond (as well as in CaF$_2$ and other homologous fluorides) has zero Raman-resonant cubic susceptibility $\chi_{1111}^{(3)R}$[38,39]. The useful anti-Stokes readout vanishes in this polarization arrangement (curve 1 in Fig. 1c). With this exception, diamond provides a vast parameter space for ultrafast broadband quantum memory with a high-contrast anti-Stokes readout (Fig. 1c).

Broadband photon wave packets

In the case of ultrashort pump, Stokes, and probe field waveforms, $E_j(t, z) = A_j(t, z)\exp[i(\beta_j z - \omega_j t)]$, $j = \text{p, r, s}$, the integration over the broadband photon packets representing these waveforms in the frequency domain, with $|\psi(z = 0)\rangle = |s, 0\rangle$ and $|\Delta\beta z| \ll 1$, yields
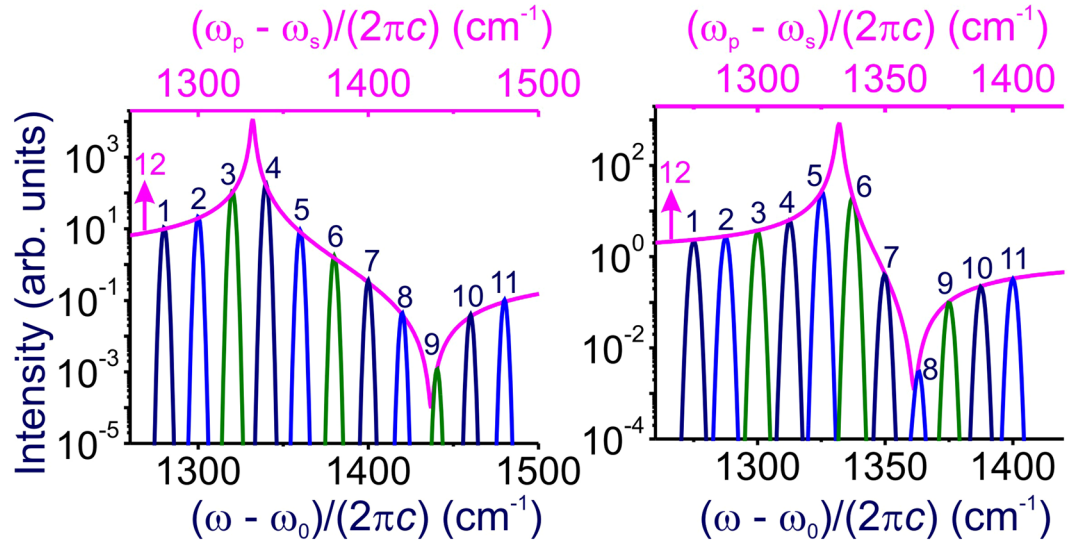
Figure 2. Spectra of the anti-Stokes readout from the $\Omega_R \approx 1332\,\text{cm}^{-1}$ zone-center $\Gamma^{(25+)}$ (F_{2g}) symmetry optical phonon in diamond driven and probed in the polarization geometry 2 (**a**) and 4 (**b**). The pulse widths of the pump and Stokes pulses are 10 ps. The central wavelength of the pump pulse is 800 nm. The pump–Stokes frequency offset $(\omega_p - \omega_s)/(2\pi c)$ is (**a**) 1280 cm^{-1} (1), 1300 cm^{-1} (2), 1320 cm^{-1} (3), 1340 cm^{-1} (4), 1360 cm^{-1} (5), 1380 cm^{-1} (6), 1400 cm^{-1} (7), 1420 cm^{-1} (8), 1440 cm^{-1} (9), 1460 cm^{-1} (10), and 1480 cm^{-1} (11); (**b**) 1275 cm^{-1} (1), 1283 cm^{-1} (2), 1300 cm^{-1} (3), 1313 cm^{-1} (4), 1325 cm^{-1} (5), 1338 cm^{-1} (6), 1350 cm^{-1} (7), 1363 cm^{-1} (8), 1375 cm^{-1} (9), 1388 cm^{-1} (10), and 1400 cm^{-1} (11). Curve 12 shows the spectrum of the anti-Stokes readout in the regime when the bandwidths of the pump, Stokes, and probe fields, Δ_p, Δ_s, and Δ_r, are much smaller than the linewidth Γ of the Raman mode.

$$\langle n_a(\omega, z) \rangle = \langle \psi(z=0) | a_a^\dagger(\omega, z) a_a(\omega, z) | \psi(z=0) \rangle$$

$$= \iint d\omega'_s d\Omega' \gamma^*(\Omega') A_p^*(\omega'_s + \Omega') A_r^*(\omega - \Omega') a_s(\omega'_s)$$

$$\iint d\omega_s d\Omega \gamma(\Omega) A_p(\omega_s + \Omega) A_r(\omega - \Omega) a_s^\dagger(\omega_s) \tag{13}$$

With the quantization rule of Eqs (3 and 13) reduces to

$$\langle n_a(\omega, z) \rangle = \int d\Omega' \gamma^*(\Omega') A_r^*(\omega - \Omega') \int d\Omega \gamma(\Omega) A_r(\omega - \Omega)$$

$$\int d\omega_s A_p^*(\omega_s + \Omega') A_p(\omega_s + \Omega) (\langle n_{s0}(\omega_s) 1 \rangle + 1) \tag{14}$$

The anti-Stokes readout of the Raman quantum memory is thus given by

$$R(\omega, z) = \int d\Omega' \gamma^*(\Omega') A_r^*(\omega - \Omega') \int d\Omega \gamma(\Omega) A_r(\omega - \Omega)$$

$$\int d\omega_s A_p^*(\omega_s + \Omega') A_p(\omega_s + \Omega) \langle n_{s0}(\omega_s) \rangle \tag{15}$$

As the first important limiting regime, we consider the case when the bandwidths of the laser pulses Δ_p and Δ_s are much smaller than the linewidth Γ of the Raman resonance,

$$\Delta_p, \Delta_s \ll \Gamma, \tag{16}$$

so that $\int d\omega_s A_p^*(\omega_s + \Omega') A_p(\omega_s + \Omega) \langle n_{s0}(\omega_s) \rangle = P_p \langle n_{s0} \rangle \delta(\Omega - \Omega_R) \delta(\Omega' - \Omega_R)$.

With the nonlinear coefficient defined by Eq. (12) with $|\chi_2/\chi_1| \ll 1$, as in the case of diamond, Eq. (15) is reduced in this regime to

$$R(\omega, z) \approx [1 + (\eta/\Gamma)^2] P_p |A_r(\omega - \Omega_R)|^2 \langle n_{s0} \rangle. \tag{17}$$

This result recovers Eq. (9) with $|\gamma|$ as defined by Eq. (12), $|\Delta\beta z| \ll 1$, and $\omega_p - \omega_s \approx \Omega_R$.

The highest contrast of the anti-Stokes signal relative to the FWM background achieved in this regime is $\sigma_0 \approx |\eta|^2/\Gamma^2$. For the 1332-cm^{-1} zone-center $\Gamma^{(25+)}$ (F_{2g}) symmetry optical phonon in diamond driven and probed in polarization arrangements 2, as shown in Fig. 1b, $\eta_2 \sim 110$ cm^{-1} and $\Gamma \sim 1$ cm^{-1} [38,39]. The highest contrast of the anti-Stokes signal in this scheme is $\sigma_0 \sim 10^4$ (Fig. 2a). For the polarization arrangement 4 (Fig. 1b), the contrast of the anti-Stokes readout is seen to be about 13 times lower (cf. Fig. 2a,b). This correlates well with the polarization
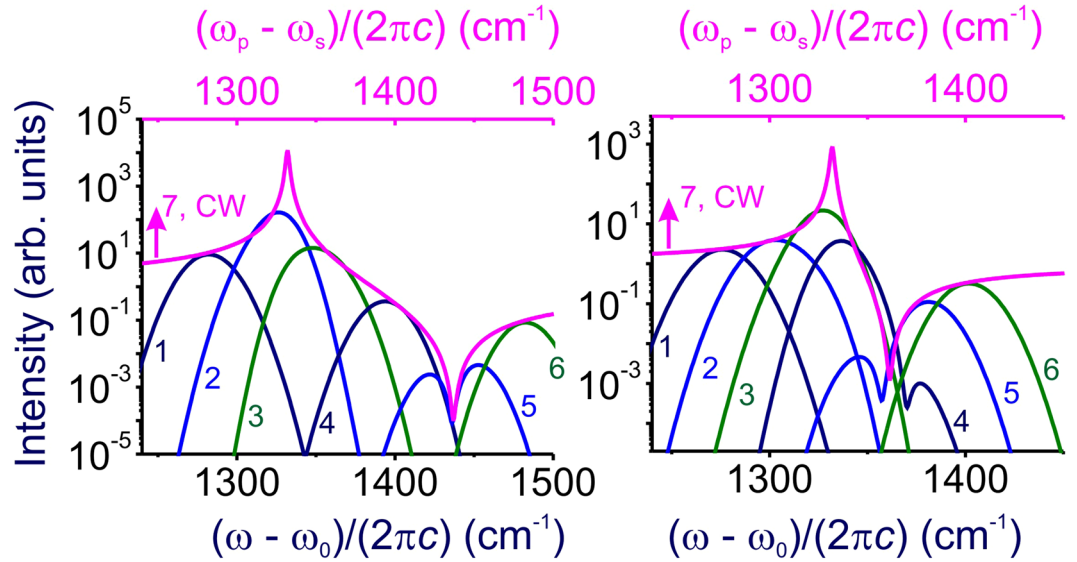
Figure 3. Spectra of the anti-Stokes readout from the $\Omega_R \approx 1332\,\mathrm{cm}^{-1}$ zone-center $\Gamma^{(25+)}$ (F_{2g}) symmetry optical phonon in diamond driven and probed in the polarization geometry 2 (**a**) and 4 (**b**). The pulse widths of the pump and Stokes pulses are 1 ps. The central wavelength of the pump pulse is 800 nm. The pump–Stokes frequency offset $(\omega_p - \omega_s)/(2\pi c)$ is (**a**) 1280 cm^{-1} (1), 1320 cm^{-1} (2), 1360 cm^{-1} (3), 1400 cm^{-1} (4), 1440 cm^{-1} (5), and 1480 cm^{-1} (6); (**b**) 1275 cm^{-1} (1), 1300 cm^{-1} (2), 1325 cm^{-1} (3), 1350 cm^{-1} (4), 1375 cm^{-1} (5), and 1400 cm^{-1} (6). Curve 7 shows the spectrum of the anti-Stokes readout in the regime when the bandwidths of the pump, Stokes, and probe fields, Δ_p, Δ_s, and Δ_r, are much smaller than the linewidth Γ of the Raman mode.

properties of the Raman response of the 1332-cm^{-1} phonon mode. Indeed, for the polarization arrangements 4, $\eta_4 \sim 30\,\mathrm{cm}^{-1}$ [38,39]. Correspondingly, the ratio of the peak values of the anti-Stokes signal in polarization geometries 2 and 4 in Fig. 1c is ~13, leading to a 13-fold difference in the highest contrast of the anti-Stokes readout for the polarization arrangements 2 and 4 in Fig. 2a,b.

As the pump–Stokes frequency difference $\omega_p - w_s$ is scanned near and through the Raman resonance $\omega_p - \omega_s = \Omega_R$, the maximum of the anti-Stokes readout in the $\Delta_p, \Delta_s \ll \Gamma$ regime closely follows the spectral profile of the Raman mode (pink curve 12 in Fig. 2a,b). In the context of ultrafast broadband quantum memory, however, such a high contrast is achieved at the expense of the operation speed. Indeed, in the case of a diamond-based quantum memory, the condition $\Delta_p, \Delta_s \ll \Gamma$ is satisfied for laser pulse widths longer than or on the order of 10 ps, which limits the memory speed to the 1–10-GHz rate level.

In the opposite limiting case, when the bandwidths of the laser pulses Δ_p, Δ_s, and Δ_r are much broader than the linewidth Γ, Eq. (15) with $|\gamma|$ as defined by Eq. (12) with $|\chi_2/\chi_1| \ll 1$ leads to

$$R(\omega, z) \approx \left[1 + \eta^2/\left(\Delta_p^2 + \Delta_s^2\right)\right]\left|A_p(\omega_p)\right|^2 \left|A_r(\omega_r)\right|^2 \langle n_{s0}\rangle. \tag{18}$$

In this case, the contrast of the anti-Stokes readout signal relative to the FWM background is a factor of $(\Delta_p^2 + \Delta_s^2)/\Gamma^2$ lower (Figs 3 and 4) than its nominally highest value, $\sigma_0 \approx |\eta|^2/\Gamma^2$. Specifically, with ~100-fs laser pulses, 10-THz operation rates can be achieved for solid-state quantum memory based on the 1332-cm^{-1} optical phonon in diamond. However, with $\Gamma \sim 1\,\mathrm{cm}^{-1}$, we find $(\Delta_p^2 + \Delta_s^2)/\Gamma^2 \sim 10^4$ for such pulse width, indicating much lower readout contrasts (Fig. 4).

Similar to their classical-field analogues, Eqs (12, 13, 15 and 17) suggest that the contrast of the anti-Stokes readout can be enhanced through a proper field-waveform tailoring. Indeed, the maximum level of the nonresonant FWM signal is achieved, as can be seen from these expressions, when the pump, Stokes, and probe pulses are all transform-limited. Resonant excitation of Raman-active phonon, on the other hand, does not necessarily require transform-limited pump and Stokes fields. Phase modulated pump and Stokes pulses can still provide a resonant excitation of a phonon mode with a central frequency Ω_R as long as their spectral phase functions $\Phi_p(\omega)$ and $\Phi_s(\omega)$ satisfy the condition[36,40] $\Phi_p(\omega) = \Phi_s(\omega - \Omega_R)$. In CARS microscopy, this condition, as elegantly shown in refs[36,40], can be satisfied by applying frequency-shifted step functions to the spectral phases of the pump and Stokes fields. The $\Phi_p(\omega) = \Phi_s(\omega - \Omega_R)$ recipe can be extended to Raman quantum information processing and storage protocols operating with quantum states of light with a well-defined phase. In the Raman scheme considered in this work, this implies a well-defined phase of the Stokes field, $\Phi_s(\omega)$. As is also readily seen from Eqs (13, 15 and 17), uncertainty in the phases of optical fields translate into fluctuations of the anti-Stokes readout. The quantum-field treatment of coherent anti-Stokes Raman scattering provided in the previous sections thus remains meaningful beyond Raman memory schemes, providing a closed formalism for a quantitative analysis of the anti-Stokes readout in coherent Raman scattering of quantum optical fields.
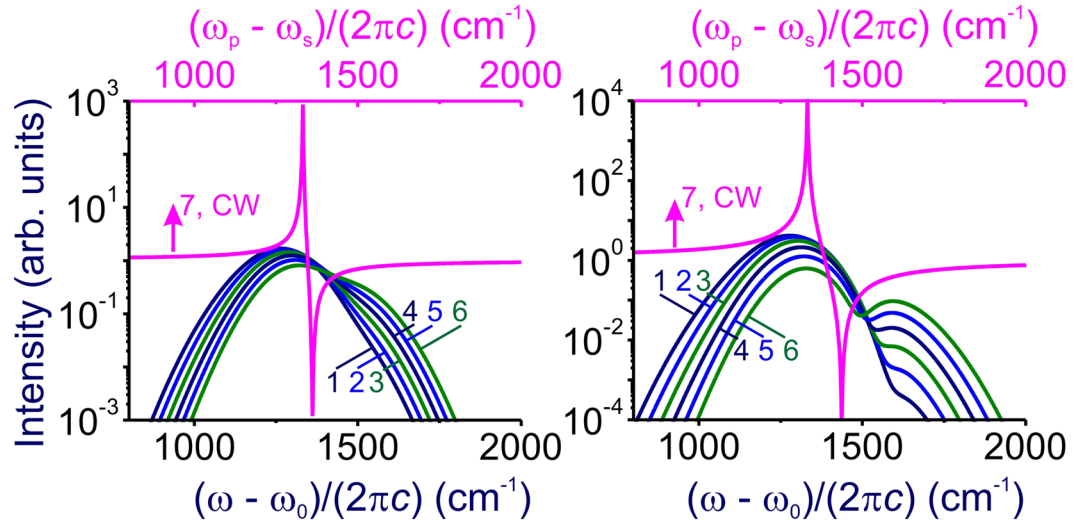
Figure 4. Spectra of the anti-Stokes readout from the $\Omega_R \approx 1332\,\text{cm}^{-1}$ zone-center $\Gamma^{(25+)}$ (F_{2g}) symmetry optical phonon in diamond driven and probed in the polarization geometry 2 (**a**) and 4 (**b**). The pulse widths of the pump and Stokes pulses are 100 fs. The central wavelength of the pump pulse is 800 nm. The pump–Stokes frequency offset $(\omega_p - \omega_s)/(2\pi c)$ is (**a**) $1280\,\text{cm}^{-1}$ (1), $1320\,\text{cm}^{-1}$ (2), $1360\,\text{cm}^{-1}$ (3), $1400\,\text{cm}^{-1}$ (4), $1440\,\text{cm}^{-1}$ (5), and $1480\,\text{cm}^{-1}$ (6); (**b**) $1275\,\text{cm}^{-1}$ (1), $1300\,\text{cm}^{-1}$ (2), $1325\,\text{cm}^{-1}$ (3), $1350\,\text{cm}^{-1}$ (4), $1375\,\text{cm}^{-1}$ (5), and $1400\,\text{cm}^{-1}$ (6). Curve 7 shows the spectrum of the anti-Stokes readout in the regime when the bandwidths of the pump, Stokes, and probe fields, Δ_p, Δ_s, and Δ_r, are much smaller than the linewidth Γ of the Raman mode.

Anti-Stokes readout with a time-delayed probe

As a powerful resource for a practical implementation of quantum memory, the probe (reading) pulse in broadband Raman memory can be applied with a variable delay time τ_d relative to the pump–Stokes write-in pulse dyad (Fig. 1a). To appreciate the advantages of this modality, it is instructive to transform the nonlinear susceptibility $\chi^{(3)}(\omega_a; \omega_p, -\omega_s, \omega_r)$, controlling, via Eq. (12), the nonlinear coefficient in the $\omega_a = \omega_p - \omega_s + \omega_r$ coherent Raman memory, to the time domain:

$$\chi^{(3)}(\omega_a; \omega_p, -\omega_s, \omega_r) = \iiint \chi^{(3)}(t_1, t_2, t_3)\exp[i(\omega_p t_1 - \omega_s t_2 + \omega_r t_3)]dt_1 dt_2 dt_3. \tag{19}$$

We isolate the Raman-resonant and FWM-nonresonant parts of the time-domain nonlinear susceptibility by representing $\chi^{(3)}(t_1, t_2, t_3)$ as

$$\chi^{(3)}(t_1, t_2, t_3) = \chi_R^{(3)}(t_1, t_2, t_3) + \chi_{nr}^{(3)}(t_1, t_2, t_3), \tag{20}$$

with

$$\chi_R^{(3)}(t_1, t_2, t_3) = \chi_R(t_1)\delta(t_2 - t_1)\delta(t_3) \tag{21}$$

and

$$\chi_{nr}^{(3)}(t_1, t_2, t_3) = \chi_{nr}\delta(t_1)\delta(t_2)\delta(t_3). \tag{22}$$

When transformed to the time domain and expressed in terms of $\chi^{(3)}(t_1, t_2, t_3)$ using Eqs (19–22), the expectation value for the anti-Stokes photon-number operator becomes

$$\langle n_a(\tau_d)\rangle \propto \int_0^\infty A_r^2(\theta - \tau_d)|q_R(\theta) + q_{nr}(\theta)|^2 d\theta, \tag{23}$$

where

$$q_R(\theta) = \int_0^\infty dt_1 \chi_r(t_1)A_p(\theta - t_1)A_s^*(\theta - t_1) \tag{24}$$

and

$$q_{nr}(\theta) = \chi_{nr}A_p(\theta)A_s^*(\theta). \tag{25}$$

As can be seen from Eqs (23–25), the anti-Stokes signal is generally a mixture of the Raman memory readout, described by the $q_R(\theta)$ term in Eq. (23), and FWM photons not related to the Raman memory and represented by the $q_{nr}(\theta)$ term in Eq. (23). However, when the pulse widths of the pump, Stokes, and probe laser pulses τ_p, τ_s, and

τ_r, are short enough, such that $\tau_p, \tau_s, \tau_r \ll 1/\Gamma$, and the delay time τ_d is chosen such that $\tau_d > \tau_p, \tau_s$, the FWM background in anti-Stokes counts is completely suppressed. Indeed, with $A_r^2(\xi) = A_r^2 \delta(\xi)$, Eq. (23) yields

$$\langle n_a(\tau_d) \rangle \propto A_r^2 \left| q_R(\tau_d) + q_{nr}(\tau_d) \right|^2. \tag{26}$$

When $\tau_d > \tau_p, \tau_s$, Eq. (26) reduces to

$$\langle n_a(\tau_d) \rangle \propto A_r^2 \left| q_R(\tau_d) \right|^2, \tag{27}$$

showing that, similar to time-resolved CARS with classical laser fields[29,41,42], the expectation value for the anti-Stokes photon-number operator $<n_a>$ measured as a function of the delay time τ_d in the quantum version of coherent Raman scattering provides a background-free map of the $|q_R(\tau_d)|^2$ trace of Raman coherence.

Remarkably, even in this mode of quantum memory, the ratio $(\Delta_p^2 + \Delta_s^2)/\Gamma^2$ is meaningful as a fundamental limit on the efficiency of Raman coherence excitation as a part of memory write-in process. Indeed, the integral

$$\Phi = \int d\Omega' \gamma^*(\Omega') \int d\Omega \gamma(\Omega) \int d\omega_s A_p^*(\omega_s + \Omega') A_p(\omega_s + \Omega) \langle n_{s0}(\omega_s) \rangle \tag{28}$$

quantifies the amplitude of the Raman coherence excited by the pump and Stokes pulses. In the case of narrow-band pump and Stokes fields, when Eq. (16) is satisfied, Eqs (12 and 28) give

$$\Phi \propto \frac{N^2 |\alpha_R|^4}{\Gamma^2} P_p \langle n_{s0} \rangle. \tag{29}$$

In the opposite limiting case of broadband pump and Stokes fields, with $\Delta_p, \Delta_s \gg \Gamma$, Eq. (28) yields

$$\Phi \propto \frac{N^2 |\alpha_R|^4}{\left(\Delta_p^2 + \Delta_s^2 \right)} P_p \langle n_{s0} \rangle. \tag{30}$$

As can be seen from Eqs (29 and 30), higher memory operation speeds are achieved at the expense of lower efficiency of Raman coherence excitation and, hence, lower amplitude of the readout signal. Moreover, the ratio of Raman coherence excitation efficiencies in the limiting cases of narrowband and broadband laser pulses is $\left(\Delta_p^2 + \Delta_s^2 \right)/\Gamma^2$.

Analysis presented above shows that ultrashort laser pulses provide a powerful resource for broadband quantum memories and, more generally, quantum information processing. In the Raman memory scheme considered here, the pump and probe (write and read) pulse widths are bounded from below by the oscillation period of the Raman-active phonon mode, $T_R = 1/(c\Omega_R)$. For the zone-center $\Gamma^{(25+)}$ (F_{2g}) symmetry optical phonon in diamond, $\Omega_R \approx 1332$-cm^{-1}, this limitation dictates $\tau_p, \tau_s, > T_R \approx 25$ fs. Pulses shorter than 25 fs are capable of inducing a Raman excitation of the 1332-cm phonon in diamond even in the absence of a quantum Stokes (signal) field.

Quantum memory corruption by noise four-wave mixing

Quantum memories based on Raman scattering[4,7–9,14,18] and electromagnetically induced transparency (EIT)[3,5,21,22] are exposed to corruption via unwanted, noise FWM pathways[43–46]. In the memory setting considered here, information stored by the Raman-active phonon may become corrupted at the write-in stage as the pump field undergoes scattering off the Raman coherence, giving rise to anti-Stokes noise photons at the frequency $\omega_a = \omega_p + \Omega_R$. In a similar FWM process, the pump field interacting with the Raman coherence at the read-out stage generates noise Stokes photons.

To understand FWM-noise-induced memory corruption in our broadband Raman memory setting, we represent the phonon coherence as a sum of the memory ($\hat{Q}$) and FWM noise ($\hat{Q}$) terms. The memory part of the Raman coherence is induced in our setting by a classical pump and a quantum Stokes field (Fig. 1a). The buildup of this coherence is governed by the quantum evolution equation (see, e.g., refs[7,30]) as dictated by the Hamitonian (4)

$$\frac{d\hat{Q}(\eta, z)}{d\eta} = ig\hat{A}_s^\dagger(\eta, z), \tag{31}$$

where η is the time in the retarded frame of reference.

The FWM noise that corrupts the memory is generated in our scheme by the pump that gets scattered off the Raman coherence, giving rise to an anti-Stokes photon. This part of Raman coherence builds up in accordance with the quantum evolution equation

$$\frac{d\hat{Q}_1(\eta, z)}{d\eta} = ig\hat{A}_a(\eta, z), \tag{32}$$

solved jointly with the equation for the anti-Stokes field generated as a result of this noise FWM,

$$\frac{d\hat{A}_a(\eta, z)}{dz} = ig\hat{Q}(\eta, z)\exp(\Delta\beta_a z), \tag{33}$$

where $\Delta\beta_a = \beta_a + \beta_s - 2\beta_p$.

It is straightforward to see from Eq. (33) that, as long as the length of the Raman-active medium, L, is chosen in such a way that $|\Delta\beta_a|L \gg 1$, anti-Stokes generation is strongly suppressed. Since the amplitude of the FWM-noise-induced anti-Stokes field controls, via Eq. (32), the buildup of the noise part of Raman coherence, large $|\Delta\beta_a|$ can radically reduce memory corruption by FWM noise.

We now expand β_a and β_s as Taylor series about ω_p:

$$\beta_a \approx \beta(\omega_p) + \frac{\Omega_R}{u_p} + \frac{\beta_2}{2}\Omega_R^2,$$ (34)

$$\beta_s \approx \beta(\omega_p) - \frac{\Omega_R}{u_p} + \frac{\beta_2}{2}\Omega_R^2,$$ (35)

where $u_p = (\partial\beta/\partial\omega)_{\omega_p}^{-1}$ is the group velocity of the pump pulse and $\beta_2 = (\partial^2\beta/\partial\omega^2)_{\omega_p}$ is the group-velocity dispersion (GVD) parameters at the pump frequency.

Using the power-series expansions of Eqs (34 and 25), we find

$$\Delta\beta_a \approx \beta_2\Omega_R^2.$$ (36)

It is now instructive to compare Raman memories based on Λ schemes in alkali-metal vapors and large-Ω_R phonons in solids with regard to the significance of phase-mismatch effects, as described by Eqs (33 and 36). For $F=1$, $m_F=0$ to $F=2$, $m_F=0$ transitions between the hyperfine-structure levels of ^{87}Rb atoms, $\Omega_{R,Rb} \approx 6.8$ GHz. For the 1332-cm^{-1} zone-center $\Gamma^{(25+)}$ (F_{2g}) symmetry optical phonon in diamond, on the other hand, $\Omega_{R,d} \approx 40$ THz. Since $|\Delta\beta_a|$ scales as Ω_R^2 [Eq. (36)], we take the ratio of these Raman shifts squared to find $\Omega_{R,d}^2/\Omega_{R,Rb}^2 \approx 3.5 \cdot 10^7$. The GVD of solids is also typically much stronger than the GVD in rarefied gas vapors, as confirmed, in a different context, by early experiments on coherent anti-Stokes Raman scattering in rare-earth-metal vapors[47,48].

Results of this qualitative analysis agree well with earlier numerical simulations[7] and, even more importantly, are fully consistent with the results of experiments[7], showing that phase mismatch can strongly suppress FWM noise in high-Ω_R diamond Raman memories. The phase-matching-enforced suppression of FWM noise and FWM-noise-induced memory corruption can be further enhanced, as pointed out in ref.[7], by dispersion engineering in microstructured waveguides. Photonic-band-gap-assisted dispersion control of coherent anti-Stokes Raman generation has been demonstrated in earlier experiments with periodically corrugated planar waveguides[49]. Diamond is fully compatible with these technologies[50].

Conclusion

To summarize, we have analyzed the tradeoff between the rate at which broadband Raman quantum memories can operate and the signal-to-noise contrast of the anti-Stokes readout from such memories. In crystalline solids, the readout contrast is strongly anisotropic, spanning many orders of magnitude for various polarization arrangements of the optical fields. Off-resonance coherent four-wave mixing has been shown to provide a source of noise photons, lowering the readout contrast in broadband Raman quantum memories. We have demonstrated that this noise cannot be suppressed by phase matching, but can be reduced by many orders of magnitude with suitable polarization arrangements and proper field-waveform tailoring.

Data availability

All data generated or analyzed during this study are included in this article.

References

1. Lvovsky, A. I., Sanders, B. C. & Tittel, W. Optical quantum memory. *Nature Photonics* **3**, 706–714 (2009).
2. Heshami, K. *et al.* Quantum memories: emerging applications and recent advances. *J. Mod. Opt.* **63**, 2005–2028 (2016).
3. Choi, K., Deng, H., Laurat, J. & Kimble, H. Mapping photonic entanglement into and out of a quantum memory. *Nature* **452**, 67–71 (2008).
4. Bustard, P. J., Lausten, R., England, D. G. & Sussman, B. J. Toward Quantum Processing in Molecules: A THz-Bandwidth Coherent Memory for Light. *Phys. Rev. Lett.* **111**, 083901 (2013).
5. Reim, K. F. *et al.* Towards high-speed optical quantum memories. *Nature Photonics* **4**, 218–221 (2010).
6. Hedges, M., Longdell, J., Li, Y. & Sellars, M. Efficient quantum memory for light. *Nature* **465**, 1052–1056 (2010).
7. England, D. G., Bustard, P. J., Nunn, J., Lausten, R. & Sussman, B. J. From Photons to Phonons and Back: A THz Optical Memory in Diamond. *Phys. Rev. Lett.* **111**, 243601 (2013).
8. Fisher, K. A. G. *et al.* Frequency and bandwidth conversion of single photons in a room-temperature diamond quantum memory. *Nature Commun.* **7**, 11200, https://doi.org/10.1038/ncomms11200 (2016).
9. England, D. G. *et al.* Storage and Retrieval of THz-Bandwidth Single Photons Using a Room-Temperature Diamond Quantum Memory. *Phys. Rev. Lett.* **114**, 053602 (2015).
10. Saunders, D. J. *et al.* Cavity-Enhanced Room-Temperature Broadband Raman Memory. *Phys. Rev. Lett.* **116**, 090501 (2016).
11. England, D. G. *et al.* Phonon-Mediated Nonclassical Interference in Diamond. *Phys. Rev. Lett.* **117**, 073603 (2016).
12. Lee, K. C. *et al.* Macroscopic non-classical states and terahertz quantum processing in room-temperature diamond. *Nature Photonics* **6**, 41–44 (2012).
13. Fisher, K. A. G. *et al.* Storage of polarization-entangled THz-bandwidth photons in a diamond quantum memory. *Phys. Rev. A* **96**, 012324 (2017).
14. Ding, D.-S. *et al.* Raman quantum memory of photonic polarized entanglement. *Nature Photonics* **9**, 332–338 (2015).
15. Zhong, M. *et al.* Optically addressable nuclear spins in a solid with a six-hour coherence time. *Nature* **517**, 177–180 (2015).
16. Bustard, P. J., England, D. G., Heshami, K., Kupchak, C. & Sussman, B. J. Reducing noise in a Raman quantum memory. *Opt. Lett.* **41**, 5055–5058 (2016).
17. Raymer, M. G. Quantum state entanglement and readout of collective atomic-ensemble modes and optical wave packets by stimulated Raman scattering. *J. Modern Opt.* **51**, 1739–1759 (2004).

18. Nunn, J. *et al*. Mapping broadband single-photon wave packets into an atomic memory. *Phys. Rev. A* **75**, 011401 (2007).
19. Parniak, M., Pęcak, D. & Wasilewski, W. Multimode Raman light-atom interface in warm atomic ensemble as multiple three-mode quantum operations. *J. Modern Opt.* **63**, 2039–2047 (2016).
20. Michelberger, P. S. *et al*. Interfacing GHz-bandwidth heralded single photons with a warm vapour. *New J. Phys.* **17**, 043006 (2015).
21. Duan, L.-M., Cirac, J. I., Zoller, P. & Polzik, E. S. Quantum Communication between Atomic Ensembles Using Coherent Light. *Phys. Rev. Lett.* **85**, 5643 (2000).
22. Julsgaard, B., Kozhekin, A. & Polzik, E. S. Experimental long-lived entanglement of two macroscopic objects. *Nature* **413**, 400 (2001).
23. Chou, C. W. *et al*. Measurement-induced entanglement for excitation stored in remote atomic ensembles. *Nature* **438**, 828–832 (2005).
24. Mitrokhin, V. P., Fedotov, A. B., Ivanov, A. A., Alfimov, M. V. & Zheltikov, A. M. Coherent anti-Stokes Raman scattering microspectroscopy of silicon components with a photonic-crystal fiber frequency shifter. *Opt. Lett.* **32**, 3471–3473 (2007).
25. Savvin, A. D., Lanin, A. A., Voronin, A. A., Fedotov, A. B. & Zheltikov, A. M. Coherent anti-Stokes Raman metrology of phonons powered by photonic-crystal fibers. *Opt. Lett.* **35**, 919–921 (2010).
26. Lanin, A. A., Fedotov, A. B. & Zheltikov, A. M. Ultrafast three-dimensional submicrometer-resolution readout of coherent optical-phonon oscillations with shaped unamplified laser pulses at 20 MHz. *Opt. Lett.* **37**, 1508–1510 (2012).
27. Lanin, A. A., Fedotov, A. B. & Zheltikov, A. M. Broadly wavelength- and pulse width-tunable high-repetition rate light pulses from soliton self-frequency shifting photonic crystal fiber integrated with a frequency doubling crystal. *Opt. Lett.* **37**, 3618–3620 (2012).
28. Shen, Y. R. *The Principles of Nonlinear Optics* (New York, Wiley, 1984).
29. Eesley, G. L. *Coherent Raman Spectroscopy* (Oxford, Pergamon, 1981).
30. Lee, K. C. *et al*. Comparing phonon dephasing lifetimes in diamond using transient coherent ultrafast spectroscopy. *Diamond Related Mater.* **19**, 1289–1295 (2010).
31. Duan, L.-M., Lukin, M. D., Cirac, J. I. & Zoller, P. Long-distance quantum communication with atomic ensembles and linear optics. *Nature* **414**, 413–418 (2001).
32. Bloembergen, N. Nonlinear optics and spectroscopy. *Rev. Mod. Phys.* **54**, 685–695 (1982).
33. McKinstrie, C. J., van Enk, S. J., Raymer, M. G. & Radic, S. Multicolor multipartite entanglement produced by vector four-wave mixing in a fiber. *Opt. Express* **16**, 2720–2739 (2008).
34. McKinstrie, C. J., Harvey, J. D., Radic, S. & Raymer, M. G. Translation of quantum states by four-wave mixing in fibers. *Opt. Express* **13**, 9131–9142 (2005).
35. McKinstrie, C. J., Yu, M., Raymer, M. G. & Radic, S. Quantum noise properties of parametric processes. *Opt. Express* **13**, 4986–5012 (2005).
36. Dudovich, N., Oron, D. & Silberberg, Y. Single-pulse coherently controlled nonlinear Raman spectroscopy and microscopy. *Nature* **418**, 512–514 (2002).
37. Zheltikov, A. M. & Koroteev, N. I. Coherent four-wave mixing in excited and ionized gas media: four-photon spectrochronography, ellipsometry, and nonlinear-optical imaging of atoms and ions. *Phys. Usp.* **42**, 321–351 (1999).
38. Levenson, M. D., Flytzanis, C. & Bloembergen, N. Interference of resonant and nonresonant three-wave mixing in diamond. *Phys. Rev. B* **6**, 3962–3965 (1972).
39. Levenson, M. D. & Bloembergen, N. Dispersion of the nonlinear optical susceptibility tensor in centrosymmetric media. *Phys. Rev. B* **10**, 4447–4463 (1974).
40. Oron, D., Dudovich, N., Yelin, D. & Silberberg, Y. Quantum control of coherent anti-Stokes Raman process. *Phys. Rev. Lett* **65**, 043408 (2002).
41. Laubereau, A. & Kaiser, W. Vibrational dynamics of liquids and solids investigated by picosecond light pulses. *Rev. Mod. Phys.* **50**, 607–668 (1978).
42. Zheltikov, A. M. Coherent anti-Stokes Raman scattering: from proof-of-the-principle experiments to femtosecond CARS and higher order wave-mixing generalizations. *J. Raman Spectrosc.* **31**, 653–667 (2000).
43. Walther, P. *et al*. Generation of narrow-bandwidth single photons using electromagnetically induced transparency in atomic ensembles. *Int. J. Quantum Inform.* **5**, 51–62 (2007).
44. Vurgaftman, I. & Bashkansky, M. Suppressing four-wave mixing in warm-atomic-vapor quantum memory. *Phys. Rev. A* **87**, 063836 (2013).
45. Zhang, K. *et al*. Suppression of the four-wave-mixing background noise in a quantum memory retrieval process by channel blocking. *Phys. Rev. A* **90**, 033823 (2014).
46. Nunn, J. *et al*. Theory of noise suppression in Λ-type quantum memories by means of a cavity. *Phys. Rev. A* **96**, 012338 (2017).
47. Gladkov, S. M., Zheltikov, A. M., Ilyasov, O. S., Koroteev, N. I. & Kulyasov, V. N. Two-photon Raman excitation: CARS study of samarium metastable-state relaxation. *Opt. Spectrosc.* **65**, 249–251 (1988).
48. Gladkov, S. M. *et al*. Strong Optical Nonlinearities of Excited Gases and Plasmas. *Proc. USSR Acad. Sci.* **52**, 217–224 (1988).
49. Konorov, S. O. *et al*. Bragg-resonance-enhanced coherent anti-Stokes Raman scattering in a planar photonic band-gap waveguide. *J. Raman Spectrosc.* **33**, 955–861 (2002).
50. Hiscocks, M. P. *et al*. Diamond waveguides fabricated by reactive ion etching. *Opt. Express* **16**, 19512–19519 (2008).

Acknowledgements

Author Contributions

A.M.Z. conceived the research, analyzed the data, and wrote the paper.

Additional Information

Competing Interests: The author declares no competing interests.

Publisher's note: Springer Nature remains neutral with regard to jurisdictional claims in published maps and institutional affiliations.